Materials Advances

ROYAL SOCIETY OF CHEMISTRY

PAPER

View Article Online
View Journal | View Issue

Cite this: *Mater. Adv.*, 2025, 6, 7282

Zinc-based metal organic framework loaded-electrospun PVA/PEO/L-arginine nanofibers as efficient antimicrobial scaffolds for burn skin wound healing

El-Refaie Kenawy,[a] Zeinab S. Ghaly,[a] Elbadawy A. Kamoun, *[bc] Wesam E. Yousuf,[d] Abdel-baset M. Shokr,[a] Youstina S. Salib[e] and Eman E. Elmohamady[f]

Burns represent a significant health challenge, causing extensive skin damage and necessitating advanced wound care strategies. This study explores the development of electrospun NFs composed of polyvinyl alcohol (PVA)/polyethylene oxide (PEO)/L-arginine (L-Arg) with a ratio of *ca.* (4 : 1 : 0.5), with/without loading zinc-based metal–organic frameworks (Zn-MOF). The synthesized Zn-MOF and the composite nanofiber were fully examined by FT-IR, XRD, SEM, and EDX analyses. Meanwhile, the incorporation effect of PEO into the PVA NFs enhanced the mechanical strength of the nanofibers, while the incorporation of Zn-MOFs enhanced the antimicrobial activity of the nanofibers. Antimicrobial testing demonstrated significant broad-spectrum efficacy *vs.* Gram-positive bacteria (*Bacillus subtilis*, *Staphylococcus aureus*), Gram-negative bacteria (*Escherichia coli*, *Klebsiella pneumoniae*), and yeast, *e.g. Candida albicans*, with the highest inhibition zones observed particularly with loading 10% Zn-MOF into the formulations. *In vivo* evaluation using a rat burn model revealed significantly accelerated wound healing, enhanced epidermal regeneration, increased wound contraction percentage, and elevated vascular endothelial growth factor (VEGF) expression in the Zn-MOF-treated groups. Histopathological analysis confirmed superior tissue regeneration and reduced inflammation, particularly for nanofibers containing high Zn-MOF concentrations. These findings indicate that Zn-MOF-loaded PVA/PEO/L-Arg nanofibers are promising candidates for the effective treatment of burn wounds, offering both antimicrobial protection and improved tissue healing.

Received 30th April 2025,
Accepted 22nd August 2025

DOI: 10.1039/d5ma00420a

rsc.li/materials-advances

1. Introduction

Burns are the most painful and physiologically incapacitating injuries, which impact almost all organ systems and result in high rates of morbidity and death.[1] The burn healing process, which includes multiple highly related and overlapping stages of inflammation, cell recruitment, matrix deposition, epithelialization, and tissue remodeling, is started by both minor burn injuries and major burn injuries. Severe big burns not only promote local wound healing but also a systemic hypermetabolic-catabolic state and a chronic pathophysiological stress response. When treating severe burn injuries, the pharmacokinetics and pharmacodynamics of medication use are significantly impacted by these pathophysiological alterations.[2] By lowering the death rate and length of hospital stay, standard clinical procedures including skin grafting and early burn wound excision have greatly improved the outcomes for patients with severe burns.[3] However, the main challenges in treating burns and research still include pain, infection, weak wound healing, and hypertrophic scarring.

Being the most common living organisms, bacteria have always posed a danger to human health before the creation of antibiotics. Infections by bacteria cause millions of deaths every year, making them a danger to public health.[4–6] Fleming in 1928, discovered the first antibiotic (*penicillin*), which transformed the management of infectious diseases by significantly lowering the rates of related mortality and morbidity.[7,8] However, antibiotic-resistant bacteria have emerged as a result of the widespread abuse and overuse of conventional antibiotics.[9,10] Many efforts have been made to produce antimicrobial

[a] *Chemistry Dep., Faculty of Science, Tanta University, Tanta, 31527, Egypt*
[b] *Department of Chemistry, College of Science, King Faisal University, Al-Ahsa, 31982, Saudi Arabia. E-mail: ekamoun@kfu.edu.sa; Tel: +20-1283320302*
[c] *Polymeric Materials Research Dep. Advanced Technology and New Materials Research Institute (ATNMRI), City of Scientific Research and Technological Applications (SRTA-City), New Borg Al-Arab City, 21934, Alexandria, Egypt*
[d] *Biochemistry Division, Chemistry Department, Faculty of Science, Tanta University, Tanta, 31527, Egypt*
[e] *Histology Department, Faculty of Medicine, Tanta University, Tanta, 31527, Egypt*
[f] *Medical Pharmacology Department, Faculty of Medicine, Tanta University, Tanta, 31527, Egypt*

drugs that can slow the proliferation of bacteria and stop the production of biofilms, and sterilize to reduce the substantial threat that bacterial infections pose to public health.[11] Because of their many functions, such as the controlled or motivated breakdown of elements that can kill bacteria, their powerful interactions with the membranes of bacteria, creation of photogenerated ROS, and their excellent loading and long-term release capabilities for additional antibacterial substances, metal organic frameworks (MOFs) have recently popped up as promising materials for various kinds of antimicrobial applications.[12] Metal–organic frameworks (MOFs) are a remarkable group of compounds where metal ions are joined by organic bridging ligands to create three-dimensional coordination networks with possible vacancies.[13] MOFs are extremely interesting because of the significant surface area and the open space that allows molecules to be captured,[14] stored, converted, and used for gas purification, energy-related technologies, heterogeneous catalysis, and sensing.[15] MOFs especially contain nickel (Ni), zinc (Zn), cobalt (Co), and copper (Cu) showing the best results as antimicrobial agents for many microbes and are regarded as biocide agents.[16] Zinc is a common, low-cost, nontoxic d-block metal used in the preparation of Zn-MOF and is included in numerous medications and cosmetics. Notably, it has antimicrobial, anti-inflammatory, astringent, and anti-dandruff qualities and functions as a cicatrizing agent and skin moisturizer.[17]

L-Arginine is an amino acid that located in most protein-rich foods, including fish, red meat, whole grains, and beans. As a supplement, L-arginine may be utilized orally and topically in wound healing.[18] The positive charge of L-arginine, giving it a known antibacterial effect, can electrostatically link with the negative charge of bacterial cells wall. The electrospinning technique creates a very fine jet that elongates, thins, and hardens as it passes across a field of electricity to a collector by using an electric potential to resist the surface tension of a solution.[19] The physics underlying the process is complicated, even though it is a somewhat easy method to carry out in a laboratory because it requires little equipment. Polymer chemistry, electric field interactions, fluid mechanics, ambient factors, and kinetics must all be taken into account to fully understand all of the variables and interactions participating in electrospinning.[20] The hydrophilic polymers poly(ethylene oxide) (PEO) and poly(vinyl alcohol) (PVA) give an excellent range of characteristics, including mechanical performance, biodegradability, biocompatibility, and non-toxicity.[21] In addition, the formation of nanofibers from PVA and PEO is easier with electrospinning techniques because of their high molecular weight and large viscosity.[22]

This study addresses the research gap of numerous published uses and methods for preparing MOFs. Despite the remarkable advancements in wound care materials, the combination of Zn-MOFs with biocompatible polymers such as PVA and PEO, further enhanced with L-Arg, has not been extensively explored for burn wound healing. Previous studies have focused individually on either MOFs' antimicrobial properties or polymeric nanofiber scaffolds, but integrating these elements into a single multifunctional electrospun dressing remains limited. In this study, we propose a novel approach by embedding Zn-MOFs into a PVA/PEO/L-Arg nanofiber matrix, aiming to synergistically combine their antimicrobial, wound-healing promotion and structural advantages. This specific composite system has not been previously reported for accelerating burn wound healing, while simultaneously offering broad-spectrum antimicrobial protection.

In this study, Zn-MOF loaded-electrospun PVA/PEO/L-Arg nanofibers were fabricated using an electrospinner, while assessing the loading effect of different contents of Zn-MOF NPs. Also, the incorporation effect of both PEO and L-Arg on the physicochemical properties and bioevalution of the composite nanofibers was studied and discussed in detail. The optimized formulation was Zn-MOF loaded PVA/PEO/L-Arg. Composite NFs were examined and assessed *in vitro* and *in vivo* in terms of their ability to be functionalized as antimicrobial biomaterials for hastening wound healing rates.

2. Materials and methods

2.1. Materials

Polyvinyl alcohol (PVA, Mwt ~60 kDa) and polyethylene oxide (PEO, Mwt ~100 kDa) were obtained from Sigma-Aldrich, Germany. L-Arginine (97%) was obtained from Nice Chemicals Pvt. Limited, India. Zinc acetate dehydrates ($(Zn(OAc)_2{\cdot}2H_2O$), 98.5%, Mwt 219.5 Da) were obtained from Techno Pharmchem, India. Terephthalic acid (dicarboxylic acid H2BDC) was obtained from PubChem, USA. *N*,*N*-Dimethylformamide (DMF, 99.9%) and ethanol (99.9%) were procured from India-MART, India. Ketamine hydrochloride and xylazine hydrochloride were obtained from KETAM, Egyptian International Pharmaceutical Industries Company (EIPICO, Egypt). The hematoxylin–eosin staining solution was obtained from Sigma Aldrich, Egypt. The biotinylated antibody was obtained from Nova Castra Laboratories Ltd, UK. Mueller–Hinton agar (MHA), Sabouraud dextrose agar (SDA), nutrient broth, and nutrient agar were obtained from Merck Chemicals Co. Germany.

2.2. Synthesis of Zn MOFs

Zn-MOFs were prepared by using the previously described method,[23] typically 0.5 g of terephthalic acid (H_2BDC, 3.05 mmol) was dissolved in 30 mL of DMF. 1.56 g ($(Zn(OAc)_2{\cdot}2H_2O$, 7.6 mmol) was dissolved in 40 mL DMF. The prepared ($(Zn(OAc)_2{\cdot}2H_2O$) solution was progressively added to the first H_2BDC solution, subsequently stirring for 20 minutes at room temperature, with a further 90 minutes of stirring. The resultant solution was centrifuged at 6000 rpm for 5 minutes. After that, the white precipitate was put into 40 mL of DMF and left overnight. Activation was carried out to exchange DMF with a volatile solvent (ethanol), then heated in an oven, and then a vacuum. The white precipitate was filtered and immersed in 40 mL of ethanol four times in two days. Subsequent to the filtration of the ethanol solution, the white precipitate was dried in an oven at 70 °C for 4 h, and subsequently activated in a vacuum at 100 °C for 8 h.[23]

2.3. Preparation of Zn-MOF loaded-PVA/PEO/Arg NFs

A PVA/PEO mixture solution (10% w/v, 4 : 1) was prepared by dissolving 0.8 g of PVA with 0.2 g of PEO in 10 mL of distilled water at 90 °C, and then letting the mixture be agitated overnight. Also, PVA/PEO/L-Arg solution was prepared by dissolving 0.08% of L-arginine in 10% PVA/PEO solution. Zn-MOF solutions were added in a different concentration of Zn-MOF (0, 2, 4, and 10%) to PVA/PEO/L-Arg solution and then sonicated for 2 h to guarantee the good dispersion of Zn-MOF in the polymeric mixture solution. For the electrospinning procedure, the composite polymeric solutions were placed in a disposable plastic syringe (10 mL) with a stainless-steel needle (0.8 mm inner diameter) employed as the solution delivery system. The cathode electrode electrospinning apparatus was attached to the plastic syringe with a stainless-steel needle. Electrospinning was performed using an applied electric potential of 21 kV (kilovoltage) with a needle-to-collector distance of 19 cm. The process was carried out in a temperature-controlled laboratory environment maintained at 32 °C, with relative humidity ranging between 45–55% under typical ambient laboratory conditions, Fig. 1. The formed nanofibers were gathered while spinning on a sheet of aluminum foil that was wrapped around a rotating collector.[24]

2.4. Instrumental characterization

An XRD model (Panalytical Empyrean 3 diffractometer, France) was used and equipped with a SolX detector utilizing Cu K radiation with a wavelength of λ = 1.542 Å. Step scanning at 2 = 0.02° per second from 5–60° was used to get the data. An FTIR model (Bruker Equinox 55, Germany) was used with a

Fig. 1 Schematic illustration of the preparation of Zn-MOF and PVA/PEO/L-Arg/Zn-MOF NFs and their possible antibacterial and tissue regeneration capacity, further leading to promoting wound healing.

Bauer EQUINOX 55 spectrometer for identifying the chemical structure, where the KBr pellet method was used to collect the spectra and the wavenumber (ν) range was 4000–400 cm^{-1}. A TGA model (Shimadzu TGA-50, Japan) was used to test the temperature stability and weight loss% at 50–800 °C, with 10 mL min^{-1} of nitrogen gas.

Instron Universal Testing Apparatus, UK was used for evaluating the mechanical strength of the nanofibers with varying MOF ratios. This measurement was carried out with ASTM D-882 guidelines for the tensile characteristics of the nanofibers. Nanofibers have properties like diameter, strain to break, and maximum stress. A computer electronic micrometer was used to find out how thick the nanofibers were. Four examples of each ready sample were looked at.

SEM model (Thermo-Fisher, Quattro S Field Emission Gun, USA), and an environmental SEM ''FEG ESEM'' with energy dispersive X-ray (EDX) capabilities, were utilized to determine the morphology of the composite nanofiber and Zn-MOFs.

A BET-specific surface area model (Quantachrome, 1900 Corporate Drive, Boynton Beach, FL 33426 USA) and nitrogen as the sorbate were used to ascertain the samples. The t-plot gave us the micropore volume and micropore area. For the samples, a density of ρ = 2.2 g cm^{-3} was utilized.

2.5. Antimicrobial activity

To evaluate the antibacterial efficacy of the produced nanofibers (PVA/PEO NFs, PVA/PEO/L-Arg/0%Zn-MOF NFs, PVA/PEO/L-Arg/2%Zn-MOF, PVA/PEO/L-Arg/5%Zn-MOF, and PVA/PEO/L-Arg/10%Zn-MOF) designated and coded as (samples 1, 2, 3, 4 and 5) accordingly, a combination of agar disc diffusion and antibiofilm analysis was employed.

2.5.1. Microorganisms and culture conditions. Antimicrobial efficacy of the nanofibers was assessed against *Bacillus subtilis* (ATCC 6633) and *Staphylococcus aureus* (ATCC 6538), which are Gram-positive bacteria, as well as *Escherichia coli* (ATCC 8739) and *Klebsiella pneumoniae* (ST627), which are Gram-negative bacteria, and *Candida albicans* (ATCC 10221), a yeast. All microbial strains were acquired from (Dep. Botany, Faculty of Science, Tanta University, Egypt), and were preserved under suitable culture conditions. *B. subtilis*, *S. aureus*, *E. coli* and *K. pneumoniae* were cultivated on Mueller–Hinton agar (MHA),[25] while *C. albicans* was preserved on Sabouraud dextrose agar (SDA).[26] The strains were grown under standard laboratory conditions before using antimicrobial assays.

2.5.2. Disc diffusion test using agar. To cultivate human infections under research, a nutrient broth medium was utilized until the turbidity reached 0.5 McFarland standard. Utilizing sterile cotton swabs, 100 microliters of microbial cultures were uniformly distributed onto nutrient agar plates. Subsequently, the discs containing the analyzed compounds were positioned atop the plates. After one day of incubation at 37 °C, the agar plates were removed. A ruler was used to quantify the inhibitory zone in millimeters (mm), which is the clear space surrounding each disc.[27]

2.5.3. Evaluation of the antibiofilm effect. To determine the nanofibers ability to inhibit biofilm formation, a microdilution technique was employed.[28] The pre-inoculums were produced by cultivating each microbial strain in a nutrient broth medium at 37 °C with shaking at 200 rpm. To ensure cultures are in the exponential growth phase, they were incubated for a further 2 h until the concentration reached (2×10^5) CFU mL^{-1}. Then, the optical density (OD) at 600 nm was determined. Each nanofiber formulation was tested for biofilm suppression by adding 100–900 μL of microbial suspensions; the control group consisted of untreated cultures. After 24 h of incubation at 37 °C with shaking, the optical density was recorded to measure microbial growth. Biofilm inhibition (%) was calculated during comparison of OD values of treated samples to the control.[29]

2.6. *In vivo* study

All *in vivo* studies were conducted with approval from the University's Ethical Research Committee (IACUC-SCI-TU-0462), and in compliance with Tanta University's institutional ethical guidelines. These recommendations cover the correct procedures for feeding, locating, and sacrificing rats in the *in vivo* tests. The starting number of rats in each group was fixed at n = 5.

2.6.1. Wound closure (%). This study was conducted on 36 male *Wistar albino* rats (150–200 gm), attained from Tanta University animal house. Before the experiment began, they were acclimated for ten days. *Ketamine* hydrochloride (40 mg kg^{-1}) and *xylazine* hydrochloride (5 mg mL^{-1}) were injected intraperitoneally into each rat to induce anesthesia. The dorsal interscapular area was then shaved with an electric razor and cleaned with a disinfectant. A metallic solid aluminum bar with a diameter of 2 cm was heated in boiling water and placed on the rat to cause a profound second-degree burn. The bar was placed in direct contact for 15 seconds on the shaved area. Then, the animals were retained individually in plastic cages, they were fed standard food & water *ad libitum* for the duration of the experiment & 12 h of light/dark cycle.[30,31] At the recording endpoints: 3rd, 7th, 14th, and 21st days post-burn, the burnt area was evaluated to calculate the wound contraction percentage as given by the formula:

$$\%\ \text{Wound contraction on day } X = \frac{(\text{area on day 0} - \text{area on day } x)}{\text{area on day 0}} \times 100. \quad (1)$$

2.6.2. Histopathological examination (H&E). After 3 weeks, skin tissue specimens were taken, fixed in formalin 10% & stained with hematoxylin & eosin. The skin specimens were taken and promptly maintained in 10% formol saline solution for one day. After that, they were dehydrated in increasing grades of ethyl alcohol and cleared in two 30-minute xylol changes. The next step was to embed in hard paraffin for two hours at 60 °C after impregnating in pure soft paraffin. Ultimately, 5 μm portions were obtained.

After sections were de-waxed and hydrated using graded alcohol, they were stained for two to five minutes with Harris' hematoxylin and then differentiated for five to ten seconds in 1% acid alcohol (1% HCL in 70% alcohol). Sections were then thoroughly cleaned for five minutes under running tap water

and stained for one to three minutes with 1% eosin. Lastly, dehydration using increasing alcohol grades, xylol clearing, and mounting with Canada balsam. The nucleus appeared in blue color while the cytoplasm appeared in pink.[32] Epidermal thickness was measured in all groups & plotted as mean ± SEM.[33]

2.6.3. Immunohistochemical staining of VEGF. After deparaffinization, sections were rehydrated and incubated in a 10% hydrogen peroxide solution for ten to fifteen minutes. Sections were microwaved in a citrate buffer solution (pH ~ 6) to retrieve the antigens for 10–20 minutes. Parts were allowed to cool for twenty minutes in a room-temperature environment. Using a buffer containing 0.05% sodium azide, the slides were washed twice. Primary antibodies were administered using monoclonal mouse anti-vascular endothelial growth factor (1 : 50) (Sigma Aldrich, Egypt). The slides were immersed in buffer four times. We used a secondary goat anti-mouse antibody that had been biotinylated. The slides were left to incubate at room temperature for ten minutes before being rinsed with buffer. A chromogen called diaminobenzidine (DAB) was used. A counterstain called Mayer's hematoxylin was employed. Rabbit kidneys were used as a positive control for anti-vascular endothelial growth factor antibody. While negative control slides were obtained by the same method, with replacement of the monoclonal antibody by saline.[34]

A morphometric study was performed at Tanta University's Histology and Cell Biology Dep., Faculty of Medicine, using an Olympus light microscope (Olympus, Japan). The software (ImageJ) program (National Institute of Health, Bethesda, Maryland, USA) was utilized. Utilizing 200× magnification, ten non-overlapping areas were taken from each slide to determine the mean color density of anti-vascular endothelial growth factor immunoreactivity.

2.6.4. Statistical analysis for *in vitro* and *in vivo* study. The results were carried out in triplicate, where data are presented as mean ± (SD). Statistical differences between groups were analyzed using one-way analysis of variance (ANOVA) and afterward *Tukey's post hoc* test for multiple comparisons. A p-value of ≤ 0.05 was regarded as statistically significant. Statistical analysis was executed using SPSS software (16.0, IBM, USA).

3. Results and discussion

3.1. Structure verification of Zn-MOF loaded-PVA/PEO/L-Arg NFs

3.1.1. FTIR analysis. Fig. 2a explains the IR spectra of pure PVA and PEO, and the hydroxyl group (OH) stretching vibrations are found to be responsible for the broadband at ν 3330 cm^{-1}.[35] In PVA, the asymmetric and symmetric stretching

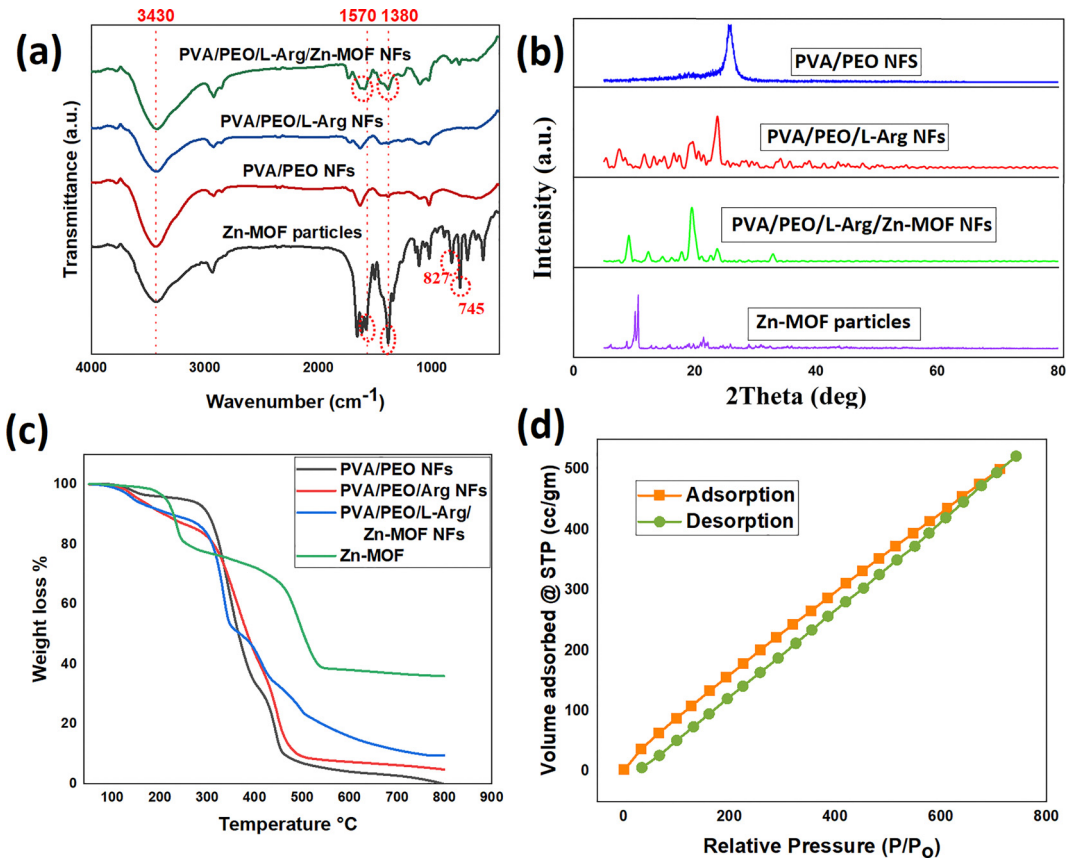

Fig. 2 FTIR spectra (a), XRD patterns of the prepared samples (b), TGA thermograph results of the prepared Zn MOF NFs (c), and N_2 sorption isotherms of the Zn MOFs (d).

vibrations of CH_2 correspond to peaks at ν 2940 and 2905 cm^{-1}, respectively, whereas in PEO the C═O and C═C stretching modes correspond to the peaks at ν 1730 and 1630 cm^{-1}.[36] The symmetrical bending of CH_2 accounted for the absorption peak at ν 1441 cm^{-1}, the band near 1094 cm^{-1} pertains to C–O stretching of the carbonyl group in the PVA backbone, and C–C stretching vibration was responsible for the peak at ν 950 cm^{-1}. The oscillation of the (OH) groups links to the peak at ν 606 cm^{-1}, while the rocking of CH_2 is associated with the peak at 916 cm^{-1}, and the bending of (CH and OH) is related to the peak at ν 1231 cm^{-1}.

FT-IR spectra of Zn-MOFs are explained in Fig. 2a, where asymmetric and symmetric stretching vibrations of the carboxylate anion $-COO^-$ from the H_2BDC linker are responsible for 2 distinctive strong bands at roughly ν 1570 and 1380 cm^{-1}, respectively.[23] The aromatic ring's C═C stretching vibration in H_2BDC, ν(C═C), is denoted by the strong peak at roughly ν 1506 cm^{-1}.[37] Aromatic C–H out-of-plane deformation vibrations, γ(C–H), in 1,4 disubstituted rings of the H_2BDC linker, are responsible for the bands at approximately ν 826 and 744 cm^{-1}.[37] The band at ν 744 cm^{-1} is significantly stronger than the band at ν 826 cm^{-1},[37] where all characteristic peaks of Zn-MOFs appear in all NFs containing Zn-MOFs, which proves the good blend between the NF composition and Zn-MOF NPs.

3.1.2. XRD analysis. The crystalline structure of the prepared PVA/PEO, PVA/PEO/L-Arg, Zn-MOF, and PVA/PEO/L-Arg/Zn MOF NFs was verified by XRD, as shown in Fig. 2b. The PVA/PEO nanofibers show two diffraction patterns at 18.78 and 27.75°,[38] which correspond to a semicrystalline polymer as shown in Fig. 2b. The XRD pattern of the PVA/PEO/L-Arg NFs shows 2θ of L-Arg at 9.19°, 12.3°, and 18.16° (ref. 39) and a peak at 26.9° for PVA/PEO, which confirms that the blending between L-Arg and polymers inside the nanofibers occurred. The XRD pattern of Zn-MOF offers 4 distinctive reflections at 2θ angles of 7.12°, 9.98°, 12.1°, and 21.2°.[40] In Fig. 2b, all present peaks confirm the complete blend of the Zn-MOF into nanofibers. The observation of a sharp peak at 7.12° signified the achievement of a highly crystalline material.[41] The peak at 2θ = 9.98° is composed of two subpeaks, suggesting that Zn MOF micro-sized crystals were formed, which is consistent with the SEM pictures as shown later. Furthermore, it is evident that this peak has the strongest intensity, confirming the Zn MOF's microcrystalline structure.[41]

3.1.3. SEM investigation. ImageJ software was employed to ascertain the average diameter distribution of the Zn-MOFs and nanofibers, as were derived from the average of 40-random investigations. The average diameter data was inspected and visualized using Origin software.[42] We examine the morphology and average diameter of the Zn-MOFs, PVA, PVA/PEO, and PVA/PEO/L-Arg NFs before and after the incorporation of Zn-MOF. The surface morphological alteration of the PVA and PVA/PEO nanofibers was recorded by SEM imaging, as shown in Fig. 3. It was observed that the average diameter of the PVA NFs is 110 ± 10 as displayed in Fig. 3(a and a1), which is greater than that of the PVA/PEO NFs of 42 ± 4, as shown in Fig. 3(a1 and b1).

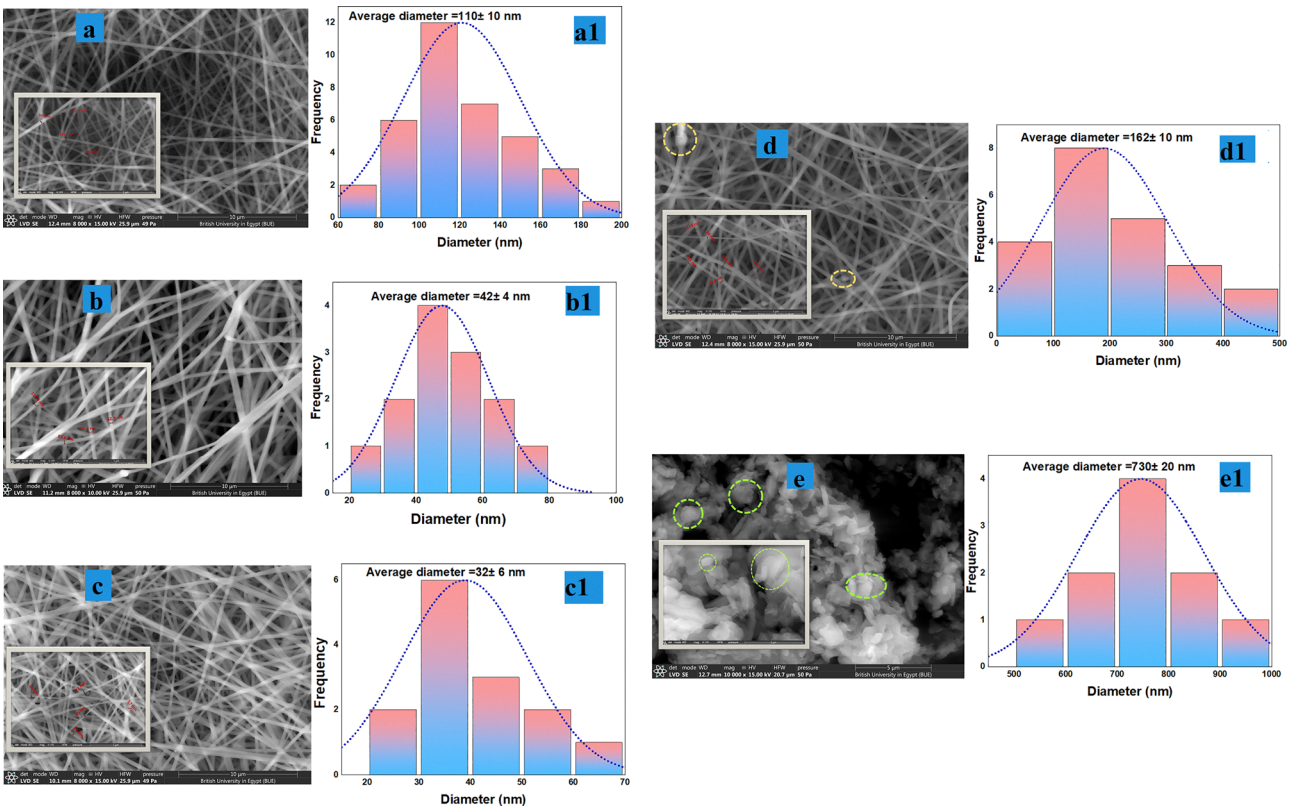

Fig. 3 SEM images of PVA NFs (a) and (a1), PVA/PEO NFs (b) and (b1), PVA/PEO/L-Arg NFs (c) and (c1), PVA/PEO/L-Arg/Zn-MOF (d) and (d1) and Zn-MOF particles (e) and (e1).

This verifies that the nanofibers are improved by incorporating PEO, because the diameter is decreased. Additionally, the nanofiber is enhanced by the addition of L-Arg, becoming 32 ± 6 nm as in Fig. 3c1. As in Fig. 3d1, the addition of Zn MOFs caused the fiber's diameter to expand to 162 ± 10 nm because of the size of its Zn-MOF nanoparticles. Images reveal that the Zn-MOFs have an irregular shape, with some spherical and needle-shaped Zn ions, where most of the Zn-MOF NP diameters are measured to be 730 ± 20 nm. The production of PVA/PEO/L-Arg/Zn-MOF nanofibers with an unknown shape was caused by high ultrasonication energy.[43]

Fig. 4a explains the elemental composition of the Zn-MOFs by EDX analysis, which verified the formation of the Zn-MOFs. These elements also appeared in different proportions, as in Table 1, which shows that the percentages of carbon, oxygen and zinc are about 54, 24 and 22%, respectively, and all this information confirms the formation of Zn-MOFs.[44]

3.1.4. Thermal measurement by TGA. TGA measurement was operated in the temperature range of 50–800 °C under gas flow of nitrogen (Fig. 2c). At temperature 50–210 °C, a progressive weight loss% is detected, which is ascribed to eliminating the water molecules that have been adsorbed on the surface of the framework of Zn-MOF.[45] Notably, at 50–300 °C, weight loss of the nanofibers is detected, due to the high moisture content in the polymers. The biggest weight loss at 210–540 °C was noticeable, which is attributed to thermal breakdown of the organic linker molecules and the production of CO_2 and benzene following the breakage of carboxylic bridges between the Zn-MOF clusters and benzene rings, where ZnO is concurrently produced in this phase.[46] Above 550 °C, the subsequent substantial weight loss is associated with ZnO carboreduction, wherein carbonaceous substances deoxidize ZnO and subsequently evaporate, mainly releasing CO_2 and CO. At 800 °C, the weight loss was almost 70%, as shown in Fig. 1b, and the decreased Zn was readily liberated from the Zn-MOF sample.

As illustrated in Fig. 2d, N_2 physical adsorption–desorption isotherms of the Zn-MOFs are typical type I isotherm profiles at a relative pressure ranging from 0.1–1.0, which represents their microporous structure. Additionally, the adsorption isotherm of the Zn-MOF reveals the type of isotherms with large constricted mesopore hysteresis loops, as also mentioned in the literature.[47] The prepared MOFs' textural parameters, such as

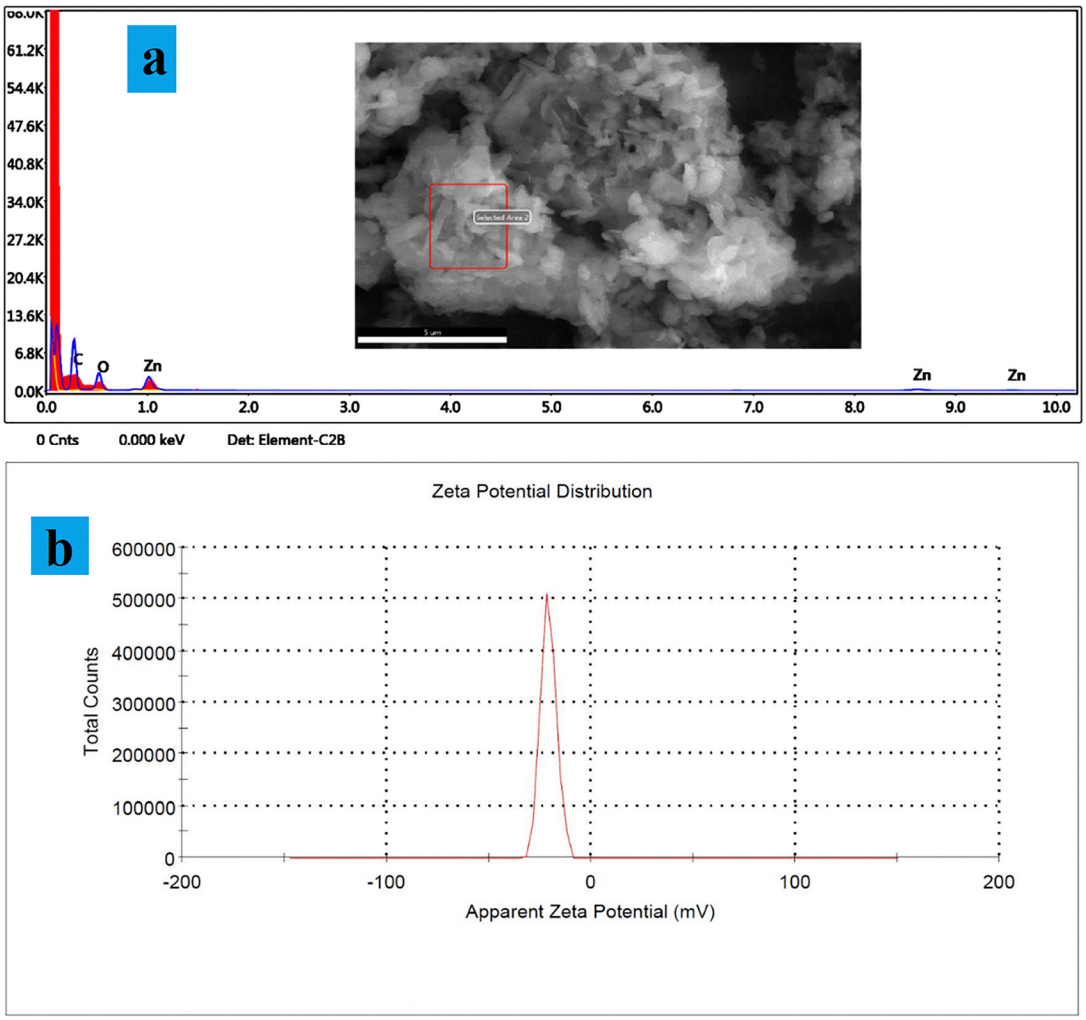

Fig. 4 EDX graph of Zn-MOFs (a) and zeta potential of Zn-MOFs (b).

Table 1 EDX elemental composition analysis of Zn-MOF

Element	Weight (%)	Atomic (%)
C	54.33	71.4
O	23.58	23.26
Zn	22.09	5.34

their BET surface area (840 m^2 g^{-1}) and average pore volume (1.6470 ± 001 nm), were determined from their N_2 adsorption–desorption isotherms at 77 K.[48]

3.1.5. Mechanical measurement. Mechanical properties of electrospun nanofiber were evaluated by tensile stress–strain values. The key tensile properties described are breaking load, tensile strength, and breaking extension.[49] Generally, PVA NFs show a loading force of about 23.33 N. After adding PEO to the PVA nanofiber composition, the nanofiber mechanicals were improved, so the strength used to cut the fiber reached about 37.99 N. With the addition of L-Arg, the SEM images show a smaller diameter, as shown in Fig. 3c. This is further evidenced by the strength of the nanofibers, as it required the highest cutting force from all samples, reaching 49.36 N. When Zn-MOFs are incorporated into the nanofibers, it leads to a weakening of the strength of the fiber, as the force used in cutting decreases. These findings are concluded as the increase in the concentration of Zn-MOFs decreases the force of the nanofiber until it reaches 11.33 N. The observed reduction in tensile strength at higher Zn-MOF concentrations can be attributed to several factors. Increased MOF loading promotes particle aggregation, creating stress concentration points that weaken the fiber structure. Additionally, the rigid MOF particles disrupt polymer chain entanglement, reducing intermolecular cohesion within the fiber matrix.[50]

Table 2 illustrates the values of mechanical measurement parameters of fabricated nanofibers with different ratios of PVA/PEO NFs and Zn-MOF. The applied force needed to cut the nanofibers increases gradually with increasing the incorporated PEO and L-Arg to NF composition. However, the overall mechanical parameters decrease significantly with incorporation of Zn-MOFs into the composite polymeric matrices.

Fig. 4b displays a graphic representation of zeta potential variations, showing that Zn-MOFs have a value of approximately −18.7 mV, indicating their anionic nature with conductivity values of 0.093 ms cm^{-1}. Meanwhile, zinc ion deposition into the framework structure is indicated by a larger negative value of zeta potential. A negative charge is localized on the MOF surface as a result of the presence of H_2BDC carboxylic groups, which might cause a negative zeta potential value.[51]

Table 2 Mechanical parameters of PVA/PEO NFs, PVA/PEO/L-Arg NFs, and PVA/PEO/L-Arg/Zn MOF composite NFs

Sample	Force (N)	Tensile stress (MPa)	Extension (mm)
PVA NFs	22.889	5.932	18.9
PVA/PEO NFs	37.99	3.8	20.4
PVA/PEO/L-Arg NFs	49.36	4.9	31.5
PVA/PEO/L-Arg/2% Zn-MOFs NFs	26.99	2.99	21.5
PVA/PEO/L-Arg/5% Zn-MOFs NFs	21.79	2.17	17
PVA/PEO/L-Arg/10% Zn-MOFs NFs	11.33	1.13	12.7

3.2. Antimicrobial activity of the nanofiber

The antimicrobial efficacy of the synthesized nanofibers was assessed using the agar disc-diffusion method against *Bacillus subtilis* (ATCC 6633) and *Staphylococcus aureus* (ATCC 6538) as examples of Gram-positive bacteria, *Escherichia coli* (ATCC 8739) and *Klebsiella pneumoniae* (ST627) as examples of Gram-negative bacteria and *Candida albicans* (ATCC 10221) as a yeast, and the inhibition zones formed are shown in Fig. 5a. The PVA/PEO/L-Arg/Zn-MOFs NFs formula (10%) exhibits the highest inhibitory effect against all microbial strains, with the most pronounced effect observed against *K. pneumoniae* ($p \leq 0.05$). These results are owing to the synergistic interaction of Zn-MOFs and L-Arg, which amplifies oxidative stress and compromises microbial cell membranes, resulting in cell death.[52] In contrast, as shown in Fig. 5b, PVA/PEO NFs exhibit the lowest antimicrobial activity, highlighting the crucial role of the incorporated L-Arg and Zn-MOFs for enhancing the bactericidal properties. Gram-negative bacteria, mainly *E. coli* and *K. pneumoniae*, demonstrate greater susceptibility to PVA/PEO/L-Arg/Zn-MOFs NFs, likened to Gram-positive bacteria. This is likely due to the Zn-MOFs creating ROSs, which effectively penetrate the outer membrane of Gram-negative bacteria.[53] Additionally, *C. albicans* shows a significant inhibition, suggesting that the tested nanofibers possess antifungal properties, making them promising candidates for combating fungal infections.

Anti-biofilm activity of nanofiber formulations was evaluated against the same microbial strains to assess their ability to prevent biofilm formation. The results are listed in Table 3, where the highest biofilm reduction was observed for PVA/PEO/L-Arg/10%Zn-MOF NFs. Meanwhile, PVA/PEO NFs exhibit minimal biofilm inhibition, ranging from 1.7–9.3%, indicating that PVA/PEO NFs alone have limited antibiofilm properties.[54] Interestingly, the incorporation of L-Arg into PVA/PEO/L-Arg NFs significantly improved the biofilm inhibition, with values ranging from 5.3–20.7%; this observation is found with all samples containing L-Arg. L-Arg likely disrupts bacterial reproduction and metabolism, inhibiting the development of biofilm formations.[55] A substantial increase in biofilm inhibition was observed with PVA/PEO/L-Arg/Zn-MOFs NFs, where the 2%Zn-MOF formulation (sample 3) achieved 55–78% inhibition, while the 5% and 10% Zn-MOF formulations (samples 4 and 5) show even greater suppression, reaching up to 93% for *K. pneumoniae*. The combined effect of Zn-MOFs and L-Arg is responsible for the enhanced antibiofilm activity of the PVA/PEO/L-Arg/Zn-MOFs NFs. It was previously reported that Zn-MOFs generate ROS that harm microbial cells, while L-Arg disrupts biofilm integrity.[56] The significant antibiofilm properties of the PVA/PEO/L-Arg/Zn-MOFs NFs indicate their potential use in avoiding biofilm-associated infections, especially in medical equipment and wound dressings.[57]

3.3. Wound contraction (%)

The wound healing process is the body's natural response to injury; it is a complex and dynamic process that allows for

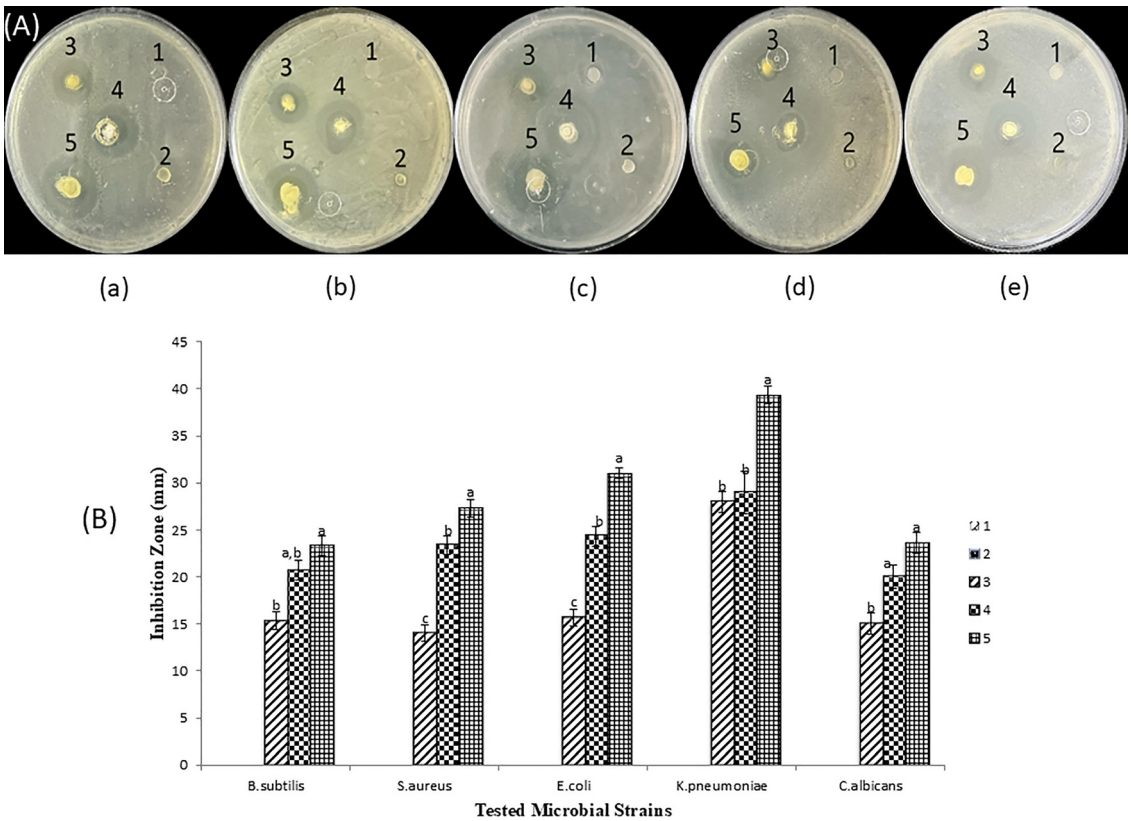

Fig. 5 (A) Antimicrobial activity of nanofibers against (a) *Bacillus subtilis* (ATCC 6633), (b) *Staphylococcus aureus* (ATCC 6538), (c) *Escherichia coli* (ATCC 8739), (d) *Klebsiella pneumoniae* (ST627) and (e) *Candida albicans* (ATCC 10221). (B) Antimicrobial activity of PVA/PEO NFs (sample 1), PVA/PEO/L-Arg NFs (sample 2), PVA/PEO/L-Arg/2% Zn MOFs NFs (sample 3), PVA/PEO/L-Arg/5% Zn MOFs NFs (sample 4) and PVA/PEO/L-Arg/10% Zn MOFs NFs (sample 5) against *B. subtilis, S. aureus, E. coli*, *K. pneumoniae* and *C. albicans* by formed inhibition zone (mm). *Data are expressed as mean ± SD (n = 3). Statistical differences were determined by one-way ANOVA followed by Tukey's *post hoc* test. $p < 0.05$ considered significant. Different letters (a, b, c) indicate statistically different groups.

Table 3 Biofilm inhibition (%) of the tested PVA/PEO NFs (sample 1), PVA/PEO/L-Arg NFs (sample 2), PVA/PEO/L-Arg/2% Zn MOFs NFs (sample 3), PVA/PEO/L-Arg/5% Zn MOFs NFs (sample 4) and PVA/PEO/L-Arg/10% Zn MOFs NFs (sample 5)

Microbial strain	Sample 1	Sample 2	Sample 3	Sample 4	Sample 5
	Biofilm inhibition zone (mm)				
B. subtilis	3.2 ± 0.17^{c}	8.5 ± 0.21^{c}	55.7 ± 0.15^{b}	84.9 ± 0.92^{a}	89.3 ± 0.38^{a}
S. aureus	2.8 ± 0.05^{c}	5.3 ± 0.19^{c}	59.5 ± 0.39^{b}	77.6 ± 3.06^{a}	85.8 ± 1.5^{a}
E. coli	1.7 ± 0.28^{c}	6.6 ± 0.22^{c}	74.2 ± 2.6^{b}	80.7 ± 3.3^{a}	90.9 ± 0.19^{a}
K. pneumoniae	2.5 ± 0.04^{c}	9.8 ± 0.04^{c}	78.5 ± 2.8^{b}	84.3 ± 0.36^{a}	93.7 ± 4.2^{a}
C. albicans	9.3 ± 0.06^{c}	20.7 ± 0.02^{c}	55.9 ± 0.24^{b}	76.2 ± 3.10^{a}	83.5 ± 0.26^{a}

*Statistical letters (a, b, c) indicate significant differences ($p \leq 0.05$) between treatments for each strain.

quick recovery of damaged tissues and normal functions. It involves four highly interconnecting and overlapping phases, including hemostasis, inflammation, proliferation, and remodeling. These phases are characterized by various physiological functions and different predominant cells at specific intervals, but great overlap might occur.[58] We highlighted the proliferation phase, particularly in our study as it involves keratinocyte migration to damaged dermis and replacement of fibrin matrix with fibroblasts that secret angiogenic factors like VEGF to form granulation tissue, which converts to new healthy extracellular matrix during the last stage.[59] Herein, we focused on deep 2nd degree burn wound healing, which involves the destruction of the epidermis, reticular dermis, and most skin appendages. This burn degree needs about 21 days to heal. We studied the wound contraction percentage on the 3rd, 7th, 14th and 21st day in the whole groups to evaluate the role of zinc embedded in PVA, PP nanofilaments in burn wound healing in addition to VEGF expression estimation at the end of the experiment as an indicator for proliferation & remodeling stages. Notably, composite NFs containing 10%Zn-MOFs (sample 5) induced a significant rapid increase in wound healing percentage & VEGF expression in comparison to all

other groups, indicating the role of arginine–zinc-loaded MOFs in enhancing angiogenesis *via* no production, which mediates the angiogenic effect of VEGF, promoting the proliferation & migration of endothelial cells. Previous reports have highlighted the role of arginine–zinc-loaded MOFs in diabetic wound healing.[60] Zinc also has antibacterial & anti-inflammatory effects that aid in burn healing besides its additional effect when combined with PVA as both of them promote the growth factors' effects like VEGF & stimulate fibroblast activity.[60,61] These findings were proved histopathologically & by epidermal thickness measurement, we found a varied area of epidermal loss with separation between the dermis and epidermis in some areas of the burn surface, with inflammatory cell aggregation in untreated groups. The polymer & arginine-treated groups showed mild improvement compared to the untreated group. However, the MOF-treated groups show compacted inflammatory cellular infiltration and the presence of thin regenerated epidermis that increased concomitantly with increased zinc concentration until reaching a maximum level in the (PVA/PEO/L-Arg/10%Zn-MOF)-treated group, in which marked regeneration with newly formed epidermis was observed.

Group 6 (PVA/PEO/L-Arg/10%Zn-MOF) shows a significant increase in wound contraction % in comparison to all other groups ($p < 0.05$) through the whole experimental period while there was a non-significant difference between group 5 (PVA/PEO/L-Arg/5%Zn-MOF), group 4 (PVA/PEO/L-Arg/2%Zn MOF) and group 3 (PVA/PEO/L-Arg) ($p > 0.05$). Still, group 5 (PVA/PEO/L-Arg/5%Zn-MOF), group 4 (PVA/PEO/L-Arg/2%Zn-MOF) and group 3 (PVA/PEO/L-Arg) display a significant improvement in wound contraction % compared to group 2 (PVA/PEO) and group 1 (untreated) ($p < 0.05$) (Fig. 6 and 7a).

3.4. Histopathological skin examination & epidermal thickness measurement (H&E ×200)

Histopathological evaluation conducted three weeks post-treatment showed distinct healing patterns across all experimental

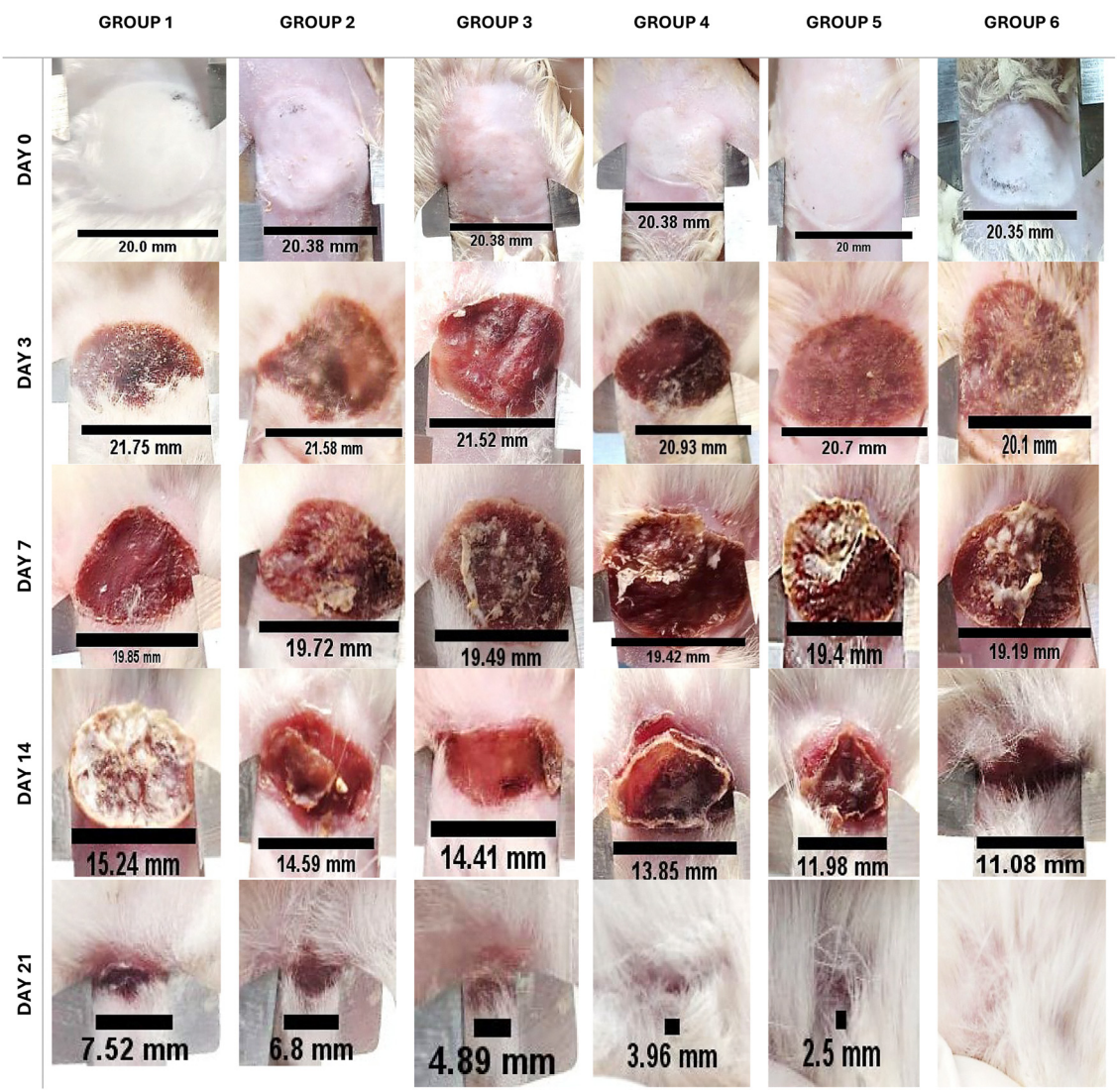

Fig. 6 Wound measurement at day 0, day 3, day 7, day 14, and day 21 of the experiment.

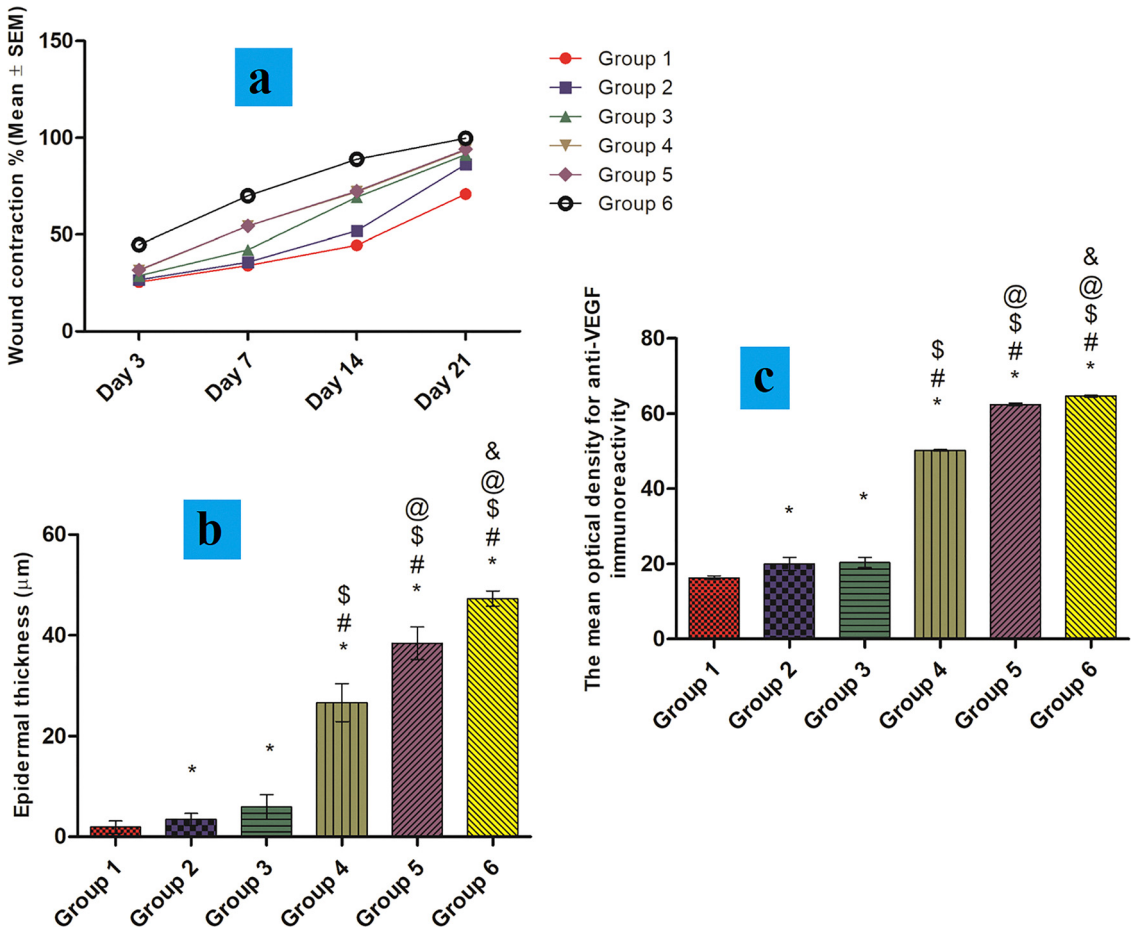

Fig. 7 Comparison between wound contraction % among different groups on day 3, day 7, day 14, and day 21 (a), epidermal thickness among different groups. Significance level = ($p < 0.05$). * = significant *vs.* group 1, # = significant *vs.* group 2, $$ = significant *vs.* group 3, @ = significant *vs.* group 4, & = significant *vs.* group 5 (b), and VEGF immunohistochemical expression among different groups. Significance level = ($p < 0.05$). * = significant *vs.* group 1, # = significant *vs.* group 2, $$ = significant *vs.* group 3, @ = significant *vs.* group 4, & = significant *vs.* group 5 (c).

groups. The control group (group 1) presented extensive epidermal damage characterized by widespread tissue loss and dermal–epidermal separation, as illustrated in Fig. 8A. Microscopic examination demonstrated substantial collagen fiber degradation, vacuolation formation and persistent inflammatory cell infiltration throughout the dermal layer. Treatment with polymer alone (group 2, Fig. 8B) showed low improvement compared to untreated burns, yet significant epidermal defects persisted alongside continued inflammatory responses. The incorporation of L-Arg (group 3, Fig. 8C) resulted in observable tissue regeneration indicators, including the formation of epidermal tongues and granulation tissue development, advising enhanced cellular proliferation and angiogenic activity. Progressive improvements were observed with increasing Zn-MOF concentrations. Group 4 (PVA/PEO/L-Arg/2%Zn-MOF) demonstrated improve granulation tissue formation and reduced inflammatory infiltrate, as shown in Fig. 8D. However, some dermal-epidermal separation remained obvious. Group 5 (PVA/PEO/L-Arg/5%Zn-MOF, Fig. 8E) exhibited superior tissue integration, with epidermal tongues maintaining closer contact with underlying dermal structures and improved vascular organization. The most notable healing response was observed in group 6 (PVA/PEO/L-Arg/10%Zn-MOF), as demonstrated in Fig. 8F. This treatment formulation promoted comprehensive epidermal regeneration with newly formed epithelial layers showing well-organized cellular architecture. While some collagen fiber loss persisted, the whole tissue morphology approached normal skin structure more closely than all other treatment groups.

Quantitative analysis of epidermal thickness measurements supported these morphological observations. Group 6 demonstrated significantly enhanced epidermal thickness compared to all other experimental groups ($p < 0.05$), as presented in Fig. 7b. Notably, all MOF-containing formulations showed statistically significant improvements in epidermal regeneration compared to treatments without zinc metal–organic framework components, indicating a dose-dependent relationship between Zn-MOF concentration and tissue healing efficacy.

3.5. Immunohistochemical analysis of VEGF (X200)

Vascular endothelial growth factor (VEGF) expression patterns varied significantly among treatment groups, reflecting different

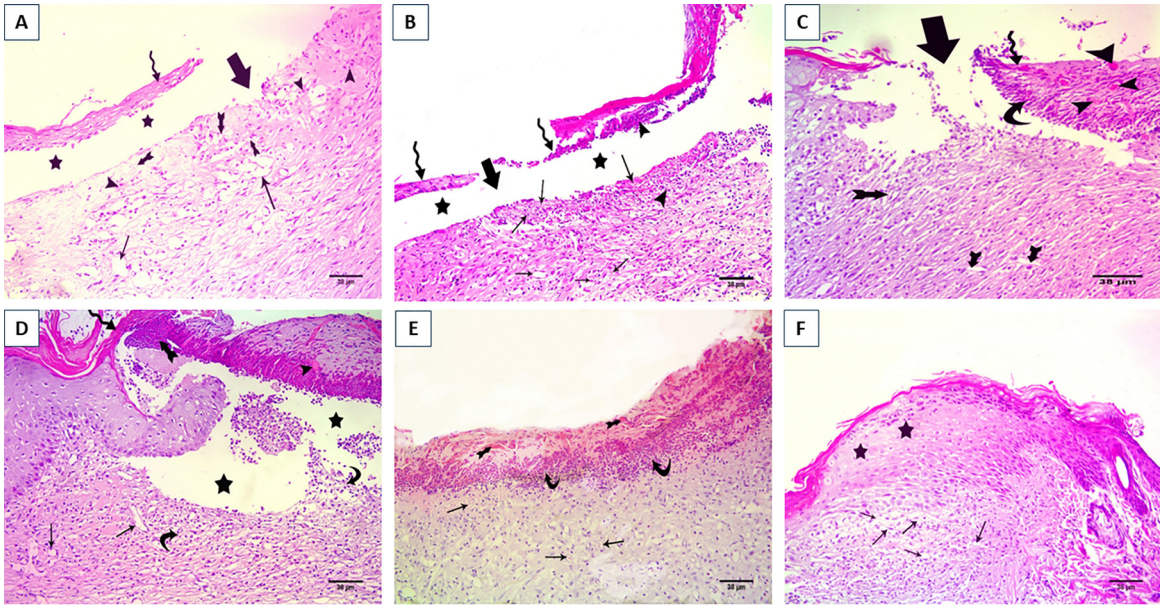

Fig. 8 Comparative histopathological examination across treatment groups. (A) Control group showing extensive epidermal loss: a graph of the untreated burn group showing a wide area of epidermal loss (thick arrow) and separation between dermis and epidermis (star). Remnants of damaged epidermis (wavy arrow). Dermis showing loss of collagen fibers and existence of vacuolations (bifid arrow), inflammatory infiltration (arrowhead) and dilated blood vessels (thin arrow). (B) Polymer treatment group: a graph of the polymer-treated group showing area of epidermal loss (thick arrow) and separation between dermis and epidermis (star). Remnants of damaged epidermis (wavy arrow) with inflammatory infiltration (arrowhead). Dermis showing loss of collagen fibers, inflammatory infiltration (arrowhead), and dilated blood vessels (thin arrow). (C) PVA/PEO/L-Arg treatment: a graph of the (PVA/PEO/L-Arg)-treated group showing an area of epidermal loss (thick arrow). Epidermal tongue (wavy arrow) with granulation tissue (arrowhead) and inflammatory infiltration (wavy arrow). Dermis showing loss of collagen fibers and dilated blood vessels (bifid arrow). (D) 2% Zn-MOF formulation: a graph of the (PVA/PEO/L-Arg/2%Zn-MOF)-treated group showing epidermal tongue (wavy arrow) with granulation tissue (arrowhead) and inflammatory infiltration (wavy arrow). Dermis showing loss of collagen fibers, dilated blood vessels (thin arrow) and inflammatory infiltration (wavy arrow). Notice the separation of the epidermal tongue from the dermis (star). (E) 5% Zn-MOF formulation: a graph of the (PVA/PEO/L-Arg/5%Zn-MOF)-treated group showing epidermal tongue with granulation tissue (bifid arrow) and inflammatory infiltration (curved arrow) in close contact with the dermis. Dermis showing loss of collagen fibers and dilated congested blood vessels (thin arrow). (F) 10% Zn-MOF formulation demonstrating optimal healing: the (PVA/PEO/L-Arg/10% Zn-MOF)-treated group showing newly formed epidermis (star). Dermis showing loss of collagen fibers and dilated blood vessels (thin arrow).

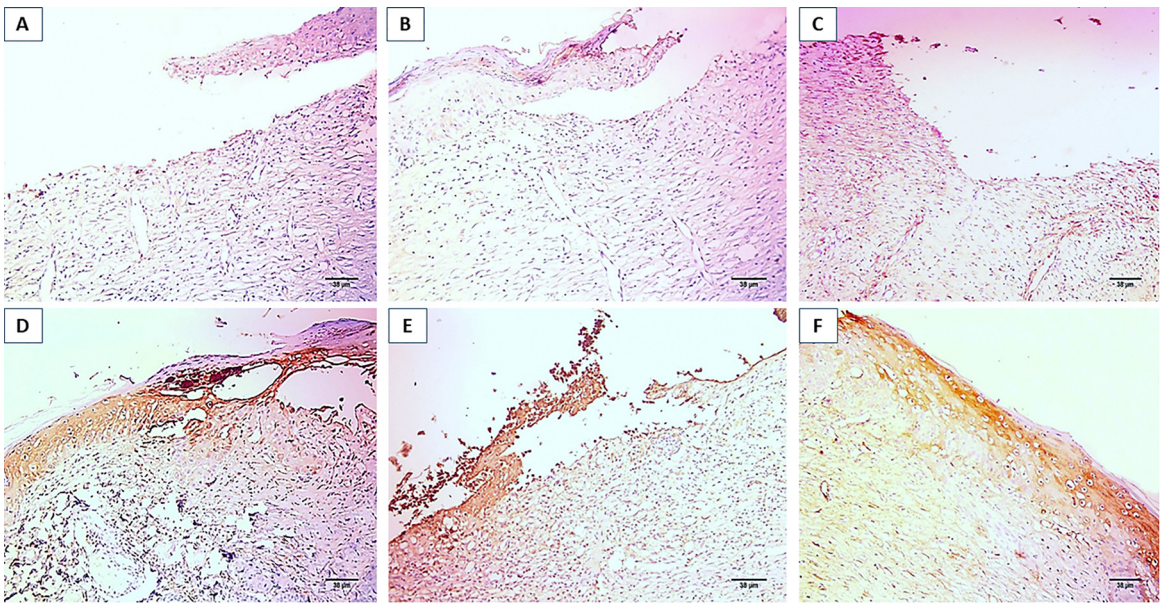

Fig. 9 VEGF immunohistochemical expression comparison: (A) control group with minimal expression; (B) polymer treatment showing weak expression; (C) L-arginine supplemented group; (D) 2% Zn-MOF formulation with mild expression; (E) 5% Zn-MOF showing moderate expression; (F) 10% Zn-MOF demonstrating maximal VEGF expression.

angiogenic potentials and healing mechanisms. The untreated control group (Fig. 9A) exhibited minimal cytoplasmic VEGF expression, indicating limited endogenous angiogenic signaling capacity in severely damaged tissue. Polymer-only treatment (group 2, Fig. 9B) and L-arginine supplementation (group 3, Fig. 9C) both demonstrated weak VEGF expression levels, suggesting modest enhancement of angiogenic pathways compared to untreated controls. These findings align with the limited morphological improvements observed in corresponding histopathological sections. The introduction of Zn-MOF components resulted in progressive increases in VEGF expression intensity. Group 4 (2% Zn-MOF, Fig. 9D) showed mild cytoplasmic VEGF expression, while group 5 (5% Zn-MOF, Fig. 9E) demonstrated moderate expression levels. This concentration-dependent response suggests that Zn-MOF incorporation enhances cellular capacity for angiogenic signaling. The highest VEGF expression was observed in group 6 (10% Zn-MOF, Fig. 9F), which displayed strong cytoplasmic immunoreactivity throughout the healing tissue. This robust VEGF expression correlates directly with the superior morphological healing observed in this group, supporting the hypothesis that enhanced angiogenesis contributes significantly to accelerated wound healing. Statistical analysis confirmed that all MOF-containing formulations demonstrated significantly elevated VEGF expression compared to treatments without zinc metal–organic framework components ($p < 0.001$), as quantified in Fig. 7C. The strong positive correlation between Zn-MOF concentration and VEGF expression suggests that the metal–organic framework components actively promote angiogenic factor production, thereby facilitating enhanced vascular network formation and tissue regeneration. These immunohistochemical findings provide mechanistic insight into the observed healing improvements, indicating that Zn-MOF incorporation enhances both cellular proliferation and vascular development through upregulation of key growth factors essential for tissue repair processes.

4. Conclusions

This study effectively generated electrospun nanofiber scaffolds made of polyvinyl alcohol (PVA), polyethylene oxide, and L-Arg, which were augmented with zinc-based metal–organic frameworks (Zn-MOFs) for burn wound healing applications. Zn-MOFs were comprehensively characterized and successfully integrated into the nanofiber (PVA/PEO/L-Arg) *via* the electrospinning method. The resultant nanofibers demonstrated consistent nanoscale shape and advantageous physical characteristics. The unloaded nanofibers exhibited negligible antimicrobial activity. However, the addition of Zn-MOFs markedly enhanced their antibacterial and antibiofilm efficacy against a wide range of pathogens. Additionally, *in vivo* assessment using a rat burn model revealed that Zn-MOF-loaded nanofibers accelerated wound contraction, improved epidermal regeneration, and stimulated VEGF production, particularly at elevated Zn-MOF concentrations. According to the results mentioned above, it is concluded that the PVA/PEO/L-Arg/10% Zn-MOF NFs could be regarded as promising with the optimal concentration for treatment of wound burns, due to their ability to enhance antibacterial defense and tissue regeneration. The results indicate that Zn-MOF-loaded PVA/PEO/L-Arg nanofibers are a promising biocompatible and multifunctional material for wound dressings in the effective treatment of burn injuries.

Ethics approval and consent to participate

All research studies followed the Helsinki World Medical Association's Declaration: Ethical Medical Research Principles Involving Human Subjects and were approved by the Ethics Committee at Tanta University in Egypt's Faculty of Science (IACUC-SCI-TU-0462).

Ethical statement

All research studies followed the Helsinki World Medical Association's Declaration: Ethical Medical Research Principles Involving Human Subjects and were approved by the ethics committee at Tanta University in Egypt's Faculty of Science.

Author contributions

Zeinab S. Ghaly, Wesam Yousuf: experiments, data analysis, wrote the original draft; Youstina Salib and Eman Elmohamady: experiments and tissue culture part; Abdel-Baset Shokr: supervision; Elbadawy A. Kamoun and El-Refaie Kenawy: study design, characterization, supervision and reviewed the original manuscript. All authors approve the current form of paper for submission.

Conflicts of interest

The authors declare no competing interests.

Data availability

The datasets used and/or analyzed during the current study are available from the corresponding author on reasonable request. In addition, all data generated or analyzed during this study are included in this article.

Acknowledgements

No funds were received for conducting this work.

References

1 R. Stone II, *et al.*, Advancements in regenerative strategies through the continuum of burn care, *Front. Pharmacol.*, 2018, **9**, 672.

2 Y. Wang, *et al.*, Burn injury: challenges and advances in burn wound healing, infection, pain and scarring, *Adv. Drug Delivery Rev.*, 2018, **123**, 3–17.
3 F. M. Wood, Skin regeneration: the complexities of translation into clinical practise, *Int. J. Biochem. Cell Biol.*, 2014, **56**, 133–140.
4 Y. Zhao, *et al.*, Pathogen infection-responsive nanoplatform targeting macrophage endoplasmic reticulum for treating life-threatening systemic infection, *Nano Res.*, 2022, **15**(7), 6243–6255.
5 J. Zhao, *et al.*, *In situ* polymerization of methylene blue on bacterial cellulose for photodynamic/photoelectricity synergistic inhibition of bacterial biofilm formation, *ACS Appl. Mater. Interfaces*, 2023, **15**(37), 43591–43606.
6 C. Gu, *et al.*, Drug-Loaded Konjac Glucomannan/Metal–Organic Framework Composite Hydrogels as Antibacterial and Anti-Inflammatory Cell Scaffolds, *ACS Appl. Mater. Interfaces*, 2023, **15**(35), 41287–41298.
7 L. Mei, *et al.*, Two-dimensional nanomaterials beyond graphene for antibacterial applications: current progress and future perspectives, *Theranostics*, 2020, **10**(2), 757.
8 Z. Wang, *et al.*, Multifunctional gold–silver–carbon quantum dots nano-hybrid composite: advancing antibacterial wound healing and cell proliferation, *ACS Appl. Mater. Interfaces*, 2023, **15**(34), 40241–40254.
9 Z. Zhou, *et al.*, Recent progress in photocatalytic antibacterial, *ACS Appl. Bio Mater.*, 2021, **4**(5), 3909–3936.
10 J. Li, *et al.*, Positively charged semiconductor conjugated polymer nanomaterials with photothermal activity for antibacterial and antibiofilm activities *in vitro* and *in vivo*, *ACS Appl. Mater. Interfaces*, 2023, **15**(34), 40864–40876.
11 Z. Chen, *et al.*, Metal-organic framework-based advanced therapeutic tools for antimicrobial applications, *Acta Biomater.*, 2024, **175**, 27–54.
12 R. Li, T. Chen and X. Pan, Metal–organic-framework-based materials for antimicrobial applications, *ACS Nano*, 2021, **15**(3), 3808–3848.
13 P. Grenni, V. Ancona and A. B. Caracciolo, Ecological effects of antibiotics on natural ecosystems: A review, *Microchem. J.*, 2018, **136**, 25–39.
14 Y. Wang, *et al.*, Metal-organic frameworks for stimuli-responsive drug delivery, *Biomaterials*, 2020, **230**, 119619.
15 H. Cai, Y.-L. Huang and D. Li, Biological metal–organic frameworks: Structures, host–guest chemistry and bioapplications, *Coord. Chem. Rev.*, 2019, **378**, 207–221.
16 M. Hubab and M. A. Al-Ghouti, Recent advances and potential applications for metal-organic framework (MOFs) and MOFs-derived materials: Characterizations and antimicrobial activities, *Biotechnol. Rep.*, 2024, e00837.
17 S. Xhafa, *et al.*, Copper and Zinc Metal–Organic Frameworks with Bipyrazole Linkers Display Strong Antibacterial Activity against Both Gram+ and Gram− Bacterial Strains, *Molecules*, 2023, **28**(16), 6160.
18 J. Zhang, *et al.*, L-Arginine carboxymethyl cellulose hydrogel releasing nitric oxide to improve wound healing, *Eur. Polym. J.*, 2023, **189**, 111940.
19 E. Kny, K. Ghosal and S. Thomas, *Electrospinning: From basic research to commercialization*, 2018, Royal Society of Chemistry.
20 M. Ahmadi Bonakdar and D. Rodrigue, Electrospinning: Processes, structures, and materials, *Macromol*, 2024, **4**(1), 58–103.
21 Q. Yang, *et al.*, PVA/PEO/PVA-g-APEG nanofiber membranes with cytocompatibility and anti-cell adhesion for biomedical applications, *Colloids Surf., A*, 2023, **657**, 130638.
22 J. Ding, *et al.*, Vapor-assisted crosslinking of a FK/PVA/PEO nanofiber membrane, *Polymers*, 2018, **10**(7), 747.
23 M. S. Biserčić, *et al.*, The quest for optimal water quantity in the synthesis of metal-organic framework MOF-5, *Microporous Mesoporous Mater.*, 2019, **278**, 23–29.
24 E.-R. Kenawy, *et al.*, Copper and fluorine-MOFs loaded-electrospun PVA/gelatin nanofibers for enhancing the antimicrobial activity of topical wound dressings: MOFs synthesis and spinning conditions optimization, *Mater. Chem. Phys.*, 2025, **332**, 130303.
25 B. M. Sieberi, *et al.*, Screening of the Dichloromethane: Methanolic Extract of Centella asiatica for Antibacterial Activities against Salmonella typhi, Escherichia coli, Shigella sonnei, Bacillus subtilis, and Staphylococcus aureus, *Sci. World J.*, 2020, **2020**(1), 6378712.
26 S. Mentese, M. T. Otkun and E. Palaz, Comparison of dichloran rose bengal chloramphenicol and Sabouraud dextrose agar with cycloheximide and chloramphenicol for airborne mold sampling, *Aerobiologia*, 2017, **33**(2), 211–219.
27 L. Buzón-Durán, R. Capita and C. Alonso-Calleja, Antibiotic susceptibility of methicillin-resistant staphylococci (MRS) of food origin: A comparison of agar disc diffusion method and a commercially available miniaturized test, *Food Microbiol.*, 2018, **72**, 220–224.
28 A. Di Salle, *et al.*, Antimicrobial and antibiofilm activity of curcumin-loaded electrospun nanofibers for the prevention of the biofilm-associated infections, *Molecules*, 2021, **26**(16), 4866.
29 E. F. Haney, M. J. Trimble and R. E. Hancock, Microtiter plate assays to assess antibiofilm activity against bacteria, *Nat. Protoc.*, 2021, **16**(5), 2615–2632.
30 Dd. S. Tavares Pereira, *et al.*, Development of animal model for studying deep second-degree thermal burns, *BioMed Res. Int.*, 2012, **2012**(1), 460841.
31 A. Yassin, *et al.*, Comparative Study of the Effects of Topically Used Insulin and Simvastatin on Thermal Induced Burn in Diabetic Albino Rats, *Med. J. Cairo Univ.*, 2018, **86**, 1837–1845.
32 S. K. Suvarna, C. Layton and J. D. Bancroft, *Theory and practice of histological techniques*, Elsevier Health Science, UK, 8th edn, 2019, pp. 126–137.
33 C. Alemdaroğlu, *et al.*, An investigation on burn wound healing in rats with chitosan gel formulation containing epidermal growth factor, *Burns*, 2006, **32**(3), 319–327.
34 T. Nguyen, *Immunohistochemistry: A Technical Guide to Current Practices*, Cambridge University Press, 1st edn, 2022, Vol. 1.

35 S. Luo, *et al.*, Excellent self-healing and antifogging coatings based on polyvinyl alcohol/hydrolyzed poly (styrene-*co*-maleic anhydride), *J. Mater. Sci.*, 2019, **54**(7), 5961–5970.
36 E. M. Abdelrazek, *et al.*, Structural, optical, morphological and thermal properties of PEO/PVP blend containing different concentrations of biosynthesized Au nanoparticles, *J. Mater. Res. Technol.*, 2018, **7**(4), 419–431.
37 N. A. Rodríguez, R. Parra and M. A. Grela, Structural characterization, optical properties and photocatalytic activity of MOF-5 and its hydrolysis products: implications on their excitation mechanism, *RSC Adv.*, 2015, **5**(89), 73112–73118.
38 M. El-Morsy, *et al.*, Optical, and electrical conductivity properties of ZnO and TiO2 nanoparticles scattered in PEO-PVA for electrical devices, *Results Phys.*, 2023, **50**, 106592.
39 C. E. Hughes, *et al.*, Elucidating the crystal structure of dl-arginine by combined powder X-ray diffraction data analysis and periodic DFT-D calculations, *Cryst. Growth Des.*, 2018, **18**(1), 42–46.
40 A. Li, *et al.*, Compositional and structural evolutions of Zn-based metal–organic frameworks during pyrolysis, *J. Phys. Chem. C*, 2018, **122**(30), 17278–17286.
41 M. Arjmandi and M. Pakizeh, Mixed matrix membranes incorporated with cubic-MOF-5 for improved polyetherimide gas separation membranes: Theory and experiment, *J. Ind. Eng. Chem.*, 2014, **20**(5), 3857–3868.
42 S. Ullah, *et al.*, Stabilized nanofibers of polyvinyl alcohol (PVA) crosslinked by unique method for efficient removal of heavy metal ions, *J. Water Process Eng.*, 2020, **33**, 101111.
43 N. K. Gupta, *et al.*, Fabrication of Zn-MOF/ZnO nanocomposites for room temperature H2S removal: Adsorption, regeneration, and mechanism, *Chemosphere*, 2021, **274**, 129789.
44 J. Panda, *et al.*, Experimental and DFT study of transition metal doping in a Zn-BDC MOF to improve electrical and visible light absorption properties, *J. Phys. Chem. C*, 2022, **126**(30), 12348–12360.
45 Y. Zhang, *et al.*, Studies on the removal of phosphate in water through adsorption using a novel Zn-MOF and its derived materials, *Arabian J. Chem.*, 2022, **15**(8), 103955.
46 Y. Kimitsuka, *et al.*, Fabrication of porous cubic architecture of ZnO using Zn-terephthalate MOFs with characteristic microstructures, *Inorg. Chem.*, 2013, **52**(24), 14028–14033.
47 X.-l Zhang, *et al.*, Ammoniated MOF-74 (Zn) derivatives as luminescent sensor for highly selective detection of tetrabromobisphenol A, *Ecotoxicol. Environ. Saf.*, 2020, **187**, 109821.
48 S. Norouzbahari, *et al.*, ZIF-8@ Zn-MOF-74 core–shell metal–organic framework (MOF) with open metal sites: Synthesis, characterization, and gas adsorption performance, *Fuel*, 2023, **339**, 127463.
49 R. N. Queiroz, P. Prediger and M. G. A. Vieira, Adsorption of polycyclic aromatic hydrocarbons from wastewater using graphene-based nanomaterials synthesized by conventional chemistry and green synthesis: a critical review, *J. Hazard. Mater.*, 2022, **422**, 126904.
50 G. W. Peterson, *et al.*, Fibre-based composites from the integration of metal–organic frameworks and polymers, *Nat. Rev. Mater.*, 2021, **6**(7), 605–621.
51 K. Arya, *et al.*, Exploration and removal of multiple metal ions using mixed-linker-architected Zn-MOF in aqueous media, *Sep. Purif. Technol.*, 2023, **307**, 122551.
52 W. Hu, *et al.*, Biomedical Metal–Organic framework materials on antimicrobial therapy: Perspectives and challenges, *Mater. Today Chem.*, 2024, **41**, 102300.
53 X. Li, *et al.*, An imine-linked metal–organic framework as a reactive oxygen species generator, *Angew. Chem., Int. Ed.*, 2021, **60**(5), 2534–2540.
54 G.-A. Junter, Thébault and L. Lebrun, Polysaccharide-based antibiofilm surfaces, *Acta Biomater.*, 2016, **30**, 13–25.
55 C. Scribani Rossi, *et al.*, Nutrient sensing and biofilm modulation: the example of L-arginine in Pseudomonas, *Int. J. Mol. Sci.*, 2022, **23**(8), 4386.
56 P. Zhang, *et al.*, An enzymatic and metal–organic framework system to prevent biofilm infections, *Cell Rep. Phys. Sci.*, 2025, **6**, 102468.
57 V. Dediu, *et al.*, Trends in photothermal nanostructures for antimicrobial applications, *Int. J. Mol. Sci.*, 2023, **24**(11), 9375.
58 M. Abazari, *et al.*, A systematic review on classification, identification, and healing process of burn wound healing, *Int. J. Lower Extremity Wounds*, 2022, **21**(1), 18–30.
59 N. Mutlu, *et al.*, Zinc improves antibacterial, anti-inflammatory and cell motility activity of chitosan for wound healing applications, *Int. J. Biol. Macromol.*, 2022, **213**, 845–857.
60 G. Xiang, *et al.*, A Zn-MOF-GOx-based cascade nanoreactor promotes diabetic infected wound healing by NO release and microenvironment regulation, *Acta Biomater.*, 2024, **182**, 245–259.
61 S. G. Jin, Production and application of biomaterials based on polyvinyl alcohol (PVA) as wound dressing, *Chem. - Asian J.*, 2022, **17**(21), e202200595.